

XtraLight-MedMamba for Classification of Neoplastic Tubular Adenomas

Aqsa Sultana, Student Member, IEEE, Rayan Afsar, Student Member, IEEE, Ahmed Rahu, MD,
 Surendra P. Singh, MD, Brian Shula, Brandon Combs, Derrick Forchetti, MD,
 Vijayan K. Asari, PhD Senior Member, IEEE

Abstract—Accurate risk stratification of precancerous polyps during routine colonoscopy screenings is essential for lowering the risk of developing colorectal cancer (CRC). However, assessment of low grade dysplasia remains limited by subjective histopathologic interpretation. Advancements in digital pathology and deep learning provide new opportunities to identify subtle and fine morphologic patterns associated with malignant progression that may be imperceptible to the human eye. In this work, we propose XtraLight-MedMamba, an ultra-lightweight state-space-based deep learning framework for classifying neoplastic tubular adenomas from whole-slide images (WSIs). The architecture is a blend of ConvNext based shallow feature extractor with parallel vision mamba to efficiently model both long- and short-range dependencies and image generalization. An integration of Spatial and Channel Attention Bridge (SCAB) module enhances multiscale feature extraction, while Fixed Non-Negative Orthogonal Classifier (FNOClassifier) enables substantial parameter reduction and improved generalization. The model was evaluated on a curated dataset acquired from patients with low-grade tubular adenomas, stratified into case and control cohorts based on subsequent CRC development. XtraLight-MedMamba achieved an accuracy of 97.18% and an F1-score of 0.9767 using approximately 32,000 parameters, outperforming transformer-based and conventional Mamba architectures with significantly higher model complexity.

Index Terms—Digital Pathology, tubular adenoma, Colorectal Cancer, parallel vision mamba, state space models, ConvNext, lightweight deep learning, whole slide images

I. INTRODUCTION

The authors would like to thank the South Bend Medical Foundation for providing access to the Neoplastic Tubular Adenomas dataset.

Aqsa Sultana and Vijayan K. Asari are with the Vision Lab and Dept. of Electrical and Computer Engineering, University of Dayton, Dayton, Ohio 45469, USA (e-mail: sultanaa3@udayton.edu; vasari1@udayton.edu).

Rayan Afsar is with the Vision Lab, University of Dayton and Dept. of Computer Science, University of Georgia, Athens, Georgia, 30605.

Ahmed Rahu, MD, is a pathology resident, and Surendra P. Singh, MD is a board-certified surgical and GI pathologist. Both are affiliated with The University of Toledo Medical Center, Toledo, Ohio, 43614

Brian Shula is with Honeywell International Inc., South Bend, Indiana, 46628

Derrick Forchetti, MD, a board certified pathologist and Brandon Combs are with the South Bend Medical Foundation, South Bend, Indiana, 46635 (email: dforchetti@sbmf.org).

The Neoplastic Tubular Adenoma (NPTA) dataset is available for download at <http://www.visionlab.udayton.edu/npta>

COLORECTAL cancer (CRC) remains a major global health challenge. It is the third most commonly diagnosed cancer and the second leading cause of cancer-related mortality in the United States [1],[2]. Colonic polyps are raised protrusions of colonic mucosa, and different types have the potential to progress to cancer. CRC most commonly arises from adenomatous polyps, well-characterized precursor (premalignant) lesions of the colonic mucosa resulting from neoplastic proliferation of glandular colonic epithelium. Although these types of polyps are benign, they carry malignant potential, capable of progressing to cancer via the adenoma-carcinoma sequence in a stepwise progression [3],[4],[5]. Over decades, the classical adenoma-carcinoma sequence has established adenomatous polyps as a central biological intermediate in colorectal tumorigenesis, forming the basis for modern CRC screening and surveillance strategies [5],[6].

Amongst the adenomatous polyps are subtypes. Tubular adenomas (TAs) represent the most prevalent subtype encountered in routine clinical practice and are therefore of particular clinical importance. The adenomatous polyps are histologically defined by their degree of dysplasia (abnormal tissue architecture) into low-grade and high-grade. In general, high-grade dysplasia is a characteristic predictor of advancement to colorectal carcinoma [3]. The majority of TAs detected via screening colonoscopy and histopathological examination typically demonstrate low-grade dysplasia, in which malignant potential is low-risk [3],[7]. Current histopathologic assessment relies primarily on subjective visual interpretation, which may be insufficient to identify subtle or spatially distributed morphologic features associated with long-term development of CRC in this ostensibly low-risk population. Epidemiologic trends further highlight the importance of improving risk stratification at the precursor lesion stage [1],[4]. Despite widespread screening initiatives among adults aged 45+ years reducing the overall incidence of CRC, important age-related disparities continue to exist; in recent years, incidence has continued to rise among younger individuals despite overall declines [1],[6]. Historical and recent data continues to highlight the continued clinical relevance of early detection and limitations in current risk assessment strategies based on coarse histologic categorization. Despite the success of screening programs in reducing CRC incidence and mortality, a significant unmet clinical need

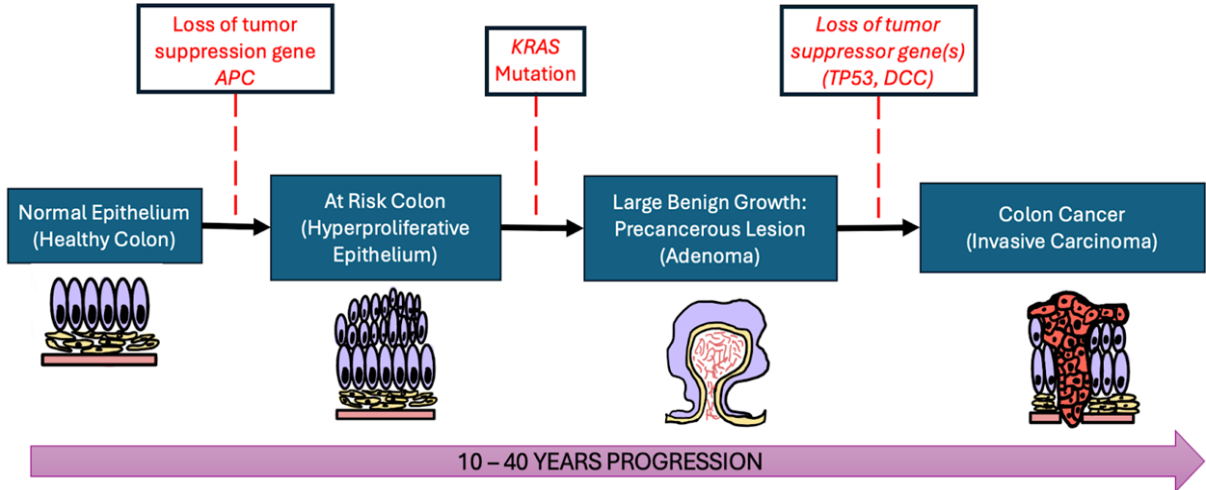


Fig. 1: Schematic illustrating the concept of the adenoma–carcinoma sequence described by Fearon and Vogelstein [5]. Simply put, the central idea is that colorectal cancer develops in a step-wise progressive manner, starting from the precursor lesions (adenomatous polyps), eventually progressing to invasive carcinoma. Early loss of APC is associated with hyperproliferative epithelium, increasing the risk of colonic polyp formation. This is followed by an activating mutation in KRAS, which itself promotes adenomatous polyp(s) formation. Subsequent loss of tumor suppressor genes, including TP53 and DCC, contributes to tumor progression and eventual neoplastic progression towards invasive colorectal adenocarcinoma [5]. This step-wise progression from adenoma(s) to cancer typically takes over ten years to progress [7].

remains in accurately stratifying risk among patients with low-grade tubular adenomas. Most individuals diagnosed with TAs are classified as low risk and managed conservatively, yet a subset will continue to later develop advanced neoplasia or CRC. Continued progress in CRC prevention will therefore require improved tools capable of extracting objective, quantitative information from precursor lesions beyond what is achievable through conventional histopathologic evaluation alone. The increasing adoption of digital pathology has transformed histopathology into a data-rich imaging modality through the routine acquisition of high-resolution whole-slide images (WSIs). When coupled with advances in machine learning, digital pathology offers the potential to enhance prophylactic efforts by enabling large-scale, quantitative analysis of tissue morphology and by uncovering subtle patterns imperceptible to human observers [8],[9]. However, the high resolution, heterogeneity, and weak labeling of WSI data introduce substantial computational challenges, necessitating efficient, scalable analytical frameworks.

Recent advances in computational pathology and deep learning architectures have enabled the automated depiction of features in the WSIs, allowing models to learn the hierarchical representation of tissue patterns directly from histologic data without the need for manual intervention. With early efforts driven by convolutional neural network (CNN)-based models [10], [11], [12], [13] and subsequently transformer-inspired models [14], [15] strong performance has been achieved by modeling local textural features and global context through self-attention mechanisms, respectively. While effective, CNNs have limited receptive

field constraining their ability to model long-range spatial relationships that are critical for understanding broader tissue architecture. Whereas, transformers incur computational overhead due to quadratic complexity, posing challenges for WSI analysis tasks.

Most recently, state space models (SSMs), have introduced new opportunities for efficient representation learning in large-scale visual data [16], [17]. Vision Mamba, [18], [19], [20] an SSM-based architecture, enables modeling of short- and long-range spatial dependencies with linear computational complexity, all while maintaining favorable computational and memory characteristics, making it well-suited for WSI analysis. In this context, the application of modern, computationally efficient architectures to digital pathology represents a critical step toward advancing cancer prevention through improved risk stratification of precursor lesions.

Conventional risk stratification methods include the categorization of adenomas based on size, histologic subtype, and grade of dysplasia, potentially overlooking finer-scale tissue patterns that may reflect underlying biological behavior. Tubular adenomas with low-grade dysplasia are often regarded as biologically homogeneous, despite evidence that not all precancerous lesions progress to malignant disease. Subtle morphologic cues and variations, such as nuclear architecture, glandular organization, and epithelial maturation, may be difficult for human observers to consistently quantify but can be captured by deep learning models. This paper proposes XtraLight-MedMamba, an ultra-lightweight parallel Mamba-based network for the classification of neoplastic tubular ade-

nomas into “case” and “control” cohorts by enhancing and identifying subtle morphologic pattern cues through the modeling of both short- and long-range spatial dependencies [21]. Through testing and evaluation, the new model, XtraLight-MedMamba, demonstrates superior performance compared to previously established models, as detailed in subsequent sections.

Our main contributions include:

- We propose a novel mamba-based extra light architecture for classification neoplastic tubular adenomas: XtraLight-MedMamba, combining the strengths of convNext block, mamba modules in parallel layers, spatial and channel attention bridge (SCAB) module and fixed non-negative orthogonal classifier (FNO-Classifier)
- The novel architecture uses (1) ConvNext blocks as a shallow feature extractor, acting upon design principles of Vision Transformers [22] (ViT) such as, depthwise separable convolutions, Layer Normalization, and MLP-style channel expansion to efficiently capture local morphologic patterns while preserving the spatial inductive bias of CNNs. (2) Parallel Vision Mamba (PVM) layers are included to parallelly model both short- and long-range spatial dependencies by branching out the features for state-space sequence modeling each with channel $C/4$, enabling efficient global contextualization of morphologic features with linear computational complexity. (3) Multiscale feature fusion is enhanced by integration of SCAB modules by emphasizing relevant informative spatial regions and channel-wise responses. (4)
- FNOClassifier is incorporated to reduce redundant parameters deeper in the layers of the model while improving generalization and training stability through structured, orthogonal feature-to-class projections.
- The effectiveness of the proposed XtraLight-MedMamba model is validated using the curated WSIs, tiled RGB images from Neoplastic Tubular Adenoma (NPTA) dataset [21].

By focusing on morphologic features critical for tissue characterization, XtraLight-MedMamba is aimed at improving the accuracy of neoplastic tubular adenoma classification by capturing subtle cellular and complex architectural patterns present in whole-slide images from case and control cohorts.

II. RELATED WORKS

Computational analysis of histopathology images has become a key research focus for improving CRC diagnosis and evaluation, driven by advances in computer vision. Early computational approaches relied on manually-developed algorithms to capture image features like texture [23] or image histograms [24], [25], followed by classical supervised learning methods like support vector machines [26], [25] or k-nearest neighbors [24]. While these methods demonstrated the feasibility of automated CRC classification, they depended on human-selected features

which may not generalize well [23] and their performance was generally lower than human pathologists [24], [25].

The emergence of CNNs for computer vision, following the success of AlexNet in 2012 [27], spurred their widespread adoption in digital pathology, including for CRC pathologies [28], [29]. CNNs have been employed for tasks like cancer detection [30], [31], [32], prognosis prediction [33], [34], and tumor grading [35], [36], [37], with performances competitive with human pathologists. More recently, Transformer-based architectures, enabled by the introduction of the Vision Transformer [22], have been explored to better capture long-range spatial relationships within colorectal tissue [38], [39], [40], and for detection of higher-order structures within CRC [41], [42]. However, transformer-based architectures rely heavily on the self-attention mechanism to capture these subtle patterns, which exhibits quadratic growth [16], [43], thus making them less suitable for use on gigapixel-sized WSIs.

Subsequently, SSM-based architectures [16] like Vision Mamba [18] have been used to great effect in digital pathology tasks like WSI image classification [44], due to their ability to capture global and local spatial context with far less computational power than transformers [45], [46]. However, most research using SSMs for histopathology tasks has been in more well-studied pathologies like lung cancer [47], [46] and breast cancer [48], [49], rather than CRC. As far as we are aware, this is the first work using a mamba-based architecture for neoplastic tubular adenoma classification in CRC histopathology slides.

III. METHODOLOGY

The XtraLight-MedMamba model adopts an architectural framework akin to convolutional neural networks (CNNs), but with a key distinction: instead of relying on convolutional blocks as its primary feature extractors, it employs Parallel Vision Mamba (PVM) layers. The overall architecture comprises six layers, with the number of channels configured as [8, 16, 24, 32, 48, 64] as shown in Fig. 2. The initial three layers utilize ConvNeXt blocks to extract shallow yet semantically rich features from whole slide image (WSI) tiles. Each ConvNeXt block follows a modernized convolutional design that replaces traditional residual bottlenecks with depthwise separable convolutions, Layer Normalization (LN), and a GELU activation-based MLP-like expansion with a 4:1 channel ratio. These design choices—originally inspired by Transformer architectures—enhance feature expressivity and optimization stability while preserving the strong spatial inductive bias characteristic of convolutional networks. The deeper layers (layers 4 through 6) incorporate PVM layers to capture more complex and nuanced features, by acting as state-space sequence mixers to efficiently model long-range dependencies across spatial regions. This hierarchical combination enables the ConvNeXt front-end to capture localized morphological patterns, while the PVM back-end contextualizes them, globally—bridging low-level texture information with high-level structural

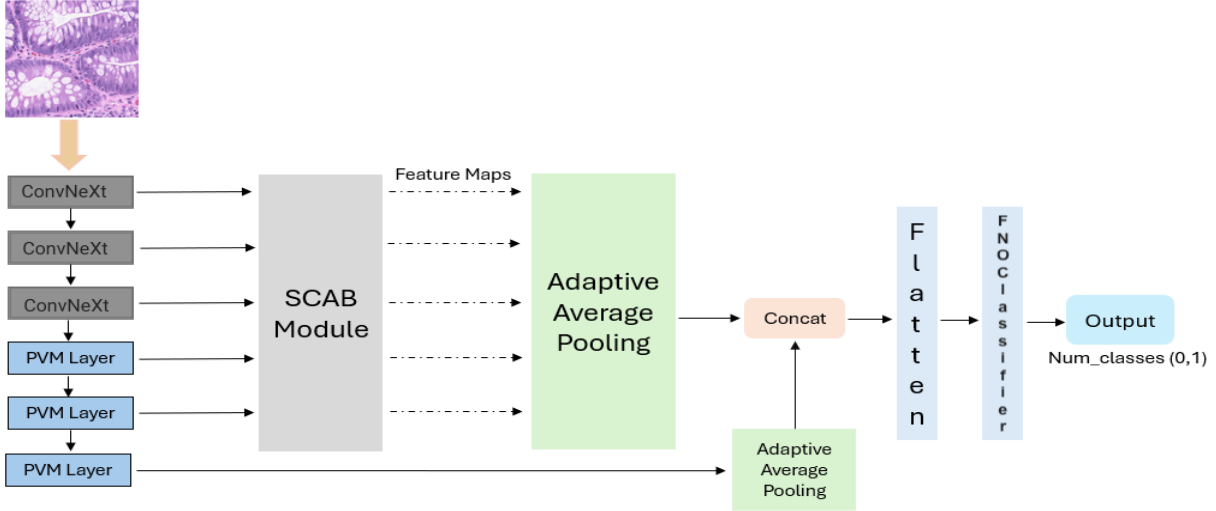


Fig. 2: Architectural structure of XtraLight-MedMamba model for image classification task. The proposed architecture consists of ConvNeXt blocks for local morphological feature extraction with PVM layers for parallel state-space modeling, spatial and channel attention as SCAB modules and FNOClassifier to enforce fixed non-negative orthogonal decision boundaries.

understanding critical for differentiating neoplastic from non-neoplastic tissue patterns.

The extracted features from three ConvNext blocks and two PVM layers are fed into a SCAB (spatial and channel attention bridge) module. Adaptive average pooling is performed on feature maps acquired from SCAB and the final PVM layer (stage 6) to standardize spatial dimensions of the feature maps. The pooled features are then concatenated to accumulate and retain the relevant information. The classification head first flattens the high-dimensional feature maps into a one-dimensional vector, effectively aggregating the spatially distributed information extracted by the preceding layers. This flattened vector is then passed through fully connected (dense) layers, which serve to map the learned feature representations to the final output space. In the case of colorectal adenoma classification, this typically corresponds to a set of class probabilities, enabling the model to assign a likelihood score to each potential category for the image: control and cancer.

A. Components of XtraLight-MedMamba Model

1) **ConvNext-Shallow Feature Extractor for XtraLight Model:** The ConvNext block [50], [51] builds upon the ResNet-style design by integrating modern architectural refinements inspired by Vision Transformer [15]. Each block begins with a 7×7 depthwise convolution that captures the long-range spatial context within each channel while maintaining computational efficiency through channel grouping, as shown in Fig. 3. The resulting feature map is then permuted from (B, C, H, W) to (B, H, W, C) to enable Layer Normalization and fully connected (linear) transformations that operate along the channel dimension, mimicking the feed-forward network structure of Transformers. This “MLP” sublayer consists

of two linear projections separated by a GELU activation, expanding the channel dimension by a factor of `mlp_ratio` before projecting it back to the original dimensionality. A learnable per-channel scaling parameter γ is applied to modulate the transformed output, followed by an inverse permutation that restores the tensor to (B, C, H, W) . Finally, a drop path is employed as a form of regularization before adding the residual connection, which preserves gradient flow and stabilizes training. This combination of depth-wise convolution, LayerNorm-based channel mixing, and residual learning enables ConvNeXt blocks to achieve high representational capacity and training stability with minimal computational overhead.

2) **Parallel Vision Mamba Module:** The PVM module [20], [52], as shown on the left side of Fig. 4 (part a), mainly consists of Mamba integrated with residual connections, which improve Mamba’s ability to capture deep spatial relationships. Initially, the input Y_{in}^C with channel C goes through layer normalization. The features that are fed into Mamba are first branched out as $X_1^{C/4}$, $X_2^{C/4}$, $X_3^{C/4}$ and $X_4^{C/4}$, each with channel $C/4$. The Mamba outputs combined with the residual connection from the inputs and adjustment factor for optimization are then concatenated together to obtain the four feature maps. The right side of Fig. 4 (part b) shows the Mamba component used in the PVM layer. These features are concatenated to obtain Y_{out}^C with the number of channels as C . The concatenated feature outputs are layer normalized and then projected using a Projection operation. By processing deep features in a parallel manner, the PVM module is able to capture multi-scale and intricate features using different kernel sizes. This process significantly reduces the parameters by retaining the same receptive field, which addresses the explosive influence of channel numbers since the number of parameters in Mamba is highly dependent on the number

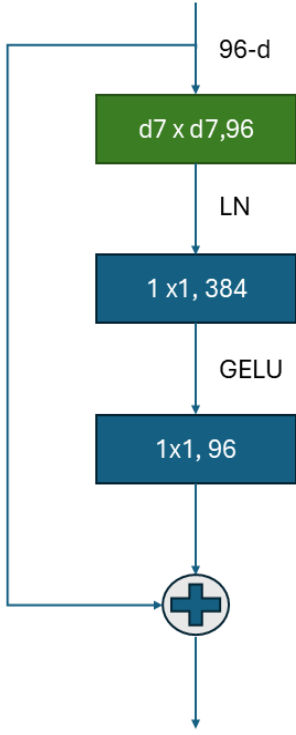


Fig. 3: Unfolded ConvNext block for Shallow Feature Extraction in XtraLight-MedMamba Model.

of input channels [52]. The specific operation can be expressed by the following equations:

$$X_{C/4}^1, X_{C/4}^2, X_{C/4}^3, X_{C/4}^4 = S_p[\text{LN}(Y_C^{\text{out}})] \quad (1)$$

$$VM_X_{C/4}^i = \text{Mamba}(X_{C/4}^i) + \theta \cdot X_{C/4}^i, \quad i = 1, 2, 3, 4 \quad (2)$$

$$Y_{\text{out}} = \text{Cat}(VM_X_1^{C/4}, VM_X_2^{C/4}, VM_X_3^{C/4}, VM_X_1^{C/4}) \quad (3)$$

$$\text{Out} = \text{Pro}[\text{LN}(Y_{\text{out}})] \quad (4)$$

Here, LN is the layer normalization, S_p is the split operation, Mamba is the Mamba operation, θ is the adjustment factor for the residual connection, Cat is the concatenation operation, and Pro is the projection operation. From Eq. 2, we employed parallel Vision Mamba feature processing while keeping the total number of channels constant, allowing us to preserve high accuracy while achieving significant parameter reduction.

3) **SCAB Module:** The model performance is further improved by the addition of the SCAB module, also known as the Spatial and Channel Attention Bridge [53], [52], for feature propagation. The spatial attention bridge consists of max-pooling, average pooling, and extended convolution of shared weights. The channel attention bridge

includes fully connected layers (FCL), global average pooling (GAP), concatenation, and a sigmoid activation function. The SCAB module enhances the sensitivity of the model, ability of the model to converge, and fusion of multi-scale features from different scales [52], [20].

4) **Fixed Non-Negative Orthogonal Classifier for Model Parameter Reduction:** The Fixed Non-Negative Orthogonal Classifier or FNOClassifier [54] module is a lightweight neural classifier designed to map feature embeddings into class logits through structured and normalized projections. During initialization, the model partitions the input feature dimensions into approximately equal groups corresponding to the number of output classes. Random permutation ensures that each class is assigned a unique subset of features, with any remaining dimensions distributed randomly among the classes to maintain balance. A binary base matrix is then constructed, where each row indicates the feature subset associated with a class, and is subsequently L2-normalized along the row dimension to enforce orthogonality and numerical stability. The model also includes an optional input feature normalization step where input vectors are scaled by their L2 norm, ensuring consistent magnitude across samples. In the forward pass, the input (normalized or raw) is linearly projected using the scaled base matrix, modulated by a learnable scalar parameter W to produce class scores. This allows the FNOClassifier to serve as an efficient and interpretable projection-based classifier, emphasizing structured feature grouping and normalization for robust classification.

Fixed classifiers that incorporate orthogonality are recognized for their cost efficiency and their capacity to sometimes outperform learnable classifiers in popular benchmarks. However, existing fixed orthogonal classifiers suffer from geometric limitations that fundamentally prevent them from invoking neural collapse [54], [55]. Inducing Neural Collapse through Fixed Non-Negative Orthogonal Classifier (FNOClassifier):

The FNOClassifier was proposed to resolve the issue that previous fixed orthogonal classifiers fail to invoke neural collapse (NC). Neural collapse is a critical phenomenon where last-layer features converge to the simplex ETF (Equiangular Tight Frame) structure necessary for achieving global optimality in a layer-peeled model, due to their inherent geometric limitations [54] [55]. The development of the FNOClassifier relies on an analysis of zero-mean NC that specifically considers orthogonality within non-negative Euclidean space. By satisfying the necessary properties of zero-mean NC, the FNOClassifier is designed to induce the optimal solution and maximize the margin of an orthogonal layer-peeled model. This classifier yields an inherent feature dimension separation effect by mitigating feature interference in continual learning and tackling the limitations of mixup on the hypersphere in imbalanced learning, ultimately demonstrating significant performance improvements across various experiments. Fixed Non-Negative Orthogonal Classifier (FNOClassifier). Let C be the number of classes and F the feature dimension. We fix a classifier with partial orthogonal

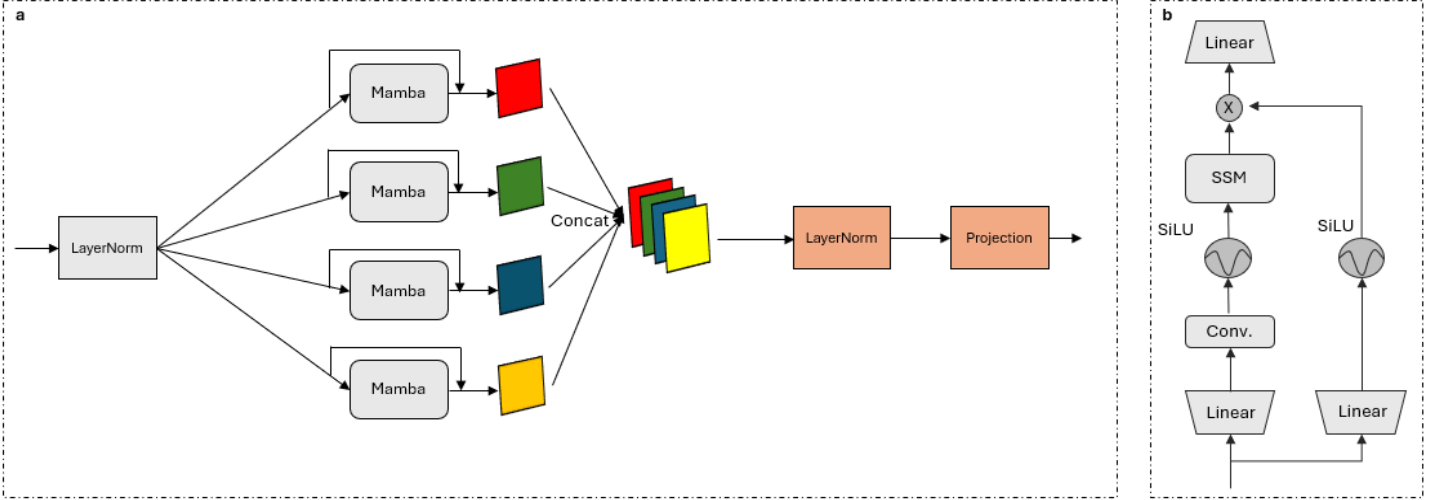


Fig. 4: a) PVM layer in XtraLight-MedMamba for capturing of both short- and long-range spatial dependencies through parallel state space modeling b) Mamba module, a selective state space model for sequence modeling with linear computational complexity.

weight matrix W as $W \in \mathbb{R}^{F \times C}$ (no learning in W) and require

$$W^\top W = I_C, \quad W_{i,j} \geq 0 \quad (\text{element-wise}), \quad (5)$$

where I_C is identity matrix and $W_{i,j}$ is the (i,j) element of W . The logits which are optionally scaled given by

$$z(x) = \gamma W^\top x \quad (\gamma > 0), \quad (6)$$

$$p(c|x) = \text{softmax}_c(z(x)). \quad (7)$$

where $z(x)$ is the logit vector, γ is a positive scaling parameter controlling the magnitude of the logits and x is the input feature representation. $p(c|x)$ is the probability predicted of an input sample with feature representation where x belongs to class c .

Neural collapse. First intra-class collapse occurs. Under zero-mean neural collapse, features from the same class converge toward a shared class mean where $x_i^{(c)}$ is the feature output of the i -th sample belonging to the class c , n_c and μ_c are the number of samples and the class mean feature vector for class c , respectively.

$$\mu_c = \frac{1}{n_c} \sum_{i=1}^{n_c} x_i^{(c)} \quad (8)$$

$$x_i^{(c)} \xrightarrow{\text{training}} \mu_c \quad (\text{intra-class collapse}) \quad (9)$$

The convergence over the course of training is denoted by $\xrightarrow{\text{training}}$. The condition in (9) indicates within-class feature variance diminishes and the same class feature embeddings concentrate around a single class.

Second, the weighted mean of the class becomes centered and converges to zero [56], [57], [58]. Therefore, the features behave as:

$$\sum_{c=1}^C \pi_c \mu_c = 0 \quad (\text{centered class means}). \quad (10)$$

In (10), C is the total number of classes, the class probability is denoted by π_c where the global feature distribution is centered at origin and the weighted average of all class means is zero.

The equal-norm constraint is given as:

$$|\mu_c| = r, \quad \forall c, \quad (11)$$

where all class means have the same Euclidean norm r .

Class-Mean Optimization. Under the neural collapse theory, feature embeddings are represented at the level of class means rather than individual samples. Training with a fixed classifier W amounts to minimizing the cross-entropy over class means μ_c :

$$\min_{\{\mu_c\}} \mathbb{E}_{c \sim \pi} \left[-\log \frac{\exp(\gamma w_c^\top \mu_c)}{\sum_{k=1}^C \exp(\gamma w_k^\top \mu_c)} \right] \quad \text{s.t.} \quad (12)$$

where, $\mathbb{E}_{c \sim \pi}$ is the class index and c is treated as a random variable according to the class probability π . w_k is the weight vector of class k and w_c is the c -th column of W for the target class. Also, with the optional constraint (11).

Margin Classification. The objective in 12 admits an equivalent max-margin formulation. Therefore, the classification margin [59] for class c against class k is expressed in a margin form:

$$\max_{\{\mu_c\}} \min_{c \neq k} (w_c^\top \mu_c - w_k^\top \mu_c) \quad \text{s.t.} \quad , \quad (13)$$

$$\|\mu_c\| = r. \quad (14)$$

Relation to simplex-ETF. In standard learnable classifiers, neural collapse theory predicts that classifier weights align with class means, i.e., $w_c \propto \mu_c$. The centered and normalized class means form a simplex equiangular tight

frame (ETF) $\langle \mu_c, \mu_{c'} \rangle$ [60], [56]:

$$\langle \mu_c, \mu_{c'} \rangle = \begin{cases} 1, & c = c', \\ -\frac{1}{C-1}, & c \neq c'. \end{cases} \quad (15)$$

However, in the FNOClassifier, W is fixed with orthonormal, non-negative columns [54], satisfying (5). As a result, optimization of (12) does not learn the classifier directions, but instead aligns with class means μ_c with the fixed directions w_c which are subject to zero-mean and equal-norm restrictions yielding a collapsed, balanced configuration without learning W .

Although the non-negativity constraint precludes an exact simplex ETF inner-product structure, the resulting geometry still enforces orthogonality of classifier directions, zero-mean centering of features, and balanced margins.

IV. EXPERIMENTAL SETUP AND RESULTS

A. Model Parameters

TABLE I: Model parameter comparison for Transformer-based models, mamba-based models with linear and fixed non-negative orthogonal classifiers.

Transformer-Based Models	Model Parameters
ViT	7,398,785
Swin Transformer	598,099
<hr/>	
Mamba-Based Models with Linear Classifier	Model Parameters
Conv. Based	49,641
MBConv. Based	59,580
Fused MBConv. Based	57,407
ConvNext Based	53,385
<hr/>	
XtraLight Mamba Models	Model Parameters
Conv. Based	28,329
MBConv. Based	38,268
Fused MBConv. Based	36,095
ConvNext Based (ours, XtraLight-MedMamba)	32,073

Table I summarizes the total number of trainable parameters across Transformer-based, Mamba-based, and XtraLight mamba-based architectures. Among Transformer models, the Vision Transformer (ViT) exhibited the highest parameter count at approximately 7.4 million, followed by the Swin Transformer with 598 thousand parameters, with their hierarchical architectural structures. In contrast, Mamba-based architectures demonstrated substantially lower complexity, with parameter counts ranging from 49 thousand to 59 thousand for linear classifier variants. Further reductions were observed in the proposed XtraLight Mamba variants, where the parameter count was reduced by nearly 40–50% compared to the baseline Mamba models. The Conv. based XtraLight Mamba model had 28,329 parameters, which was the lowest count observed. Our ConvNeXt-based model, XtraLight-MedMamba, had the second-lowest count of the models studied, at only 32,073 parameters. This underscores the effectiveness of our proposed lightweight design in minimizing computational cost while maintaining strong representational performance.

B. Dataset

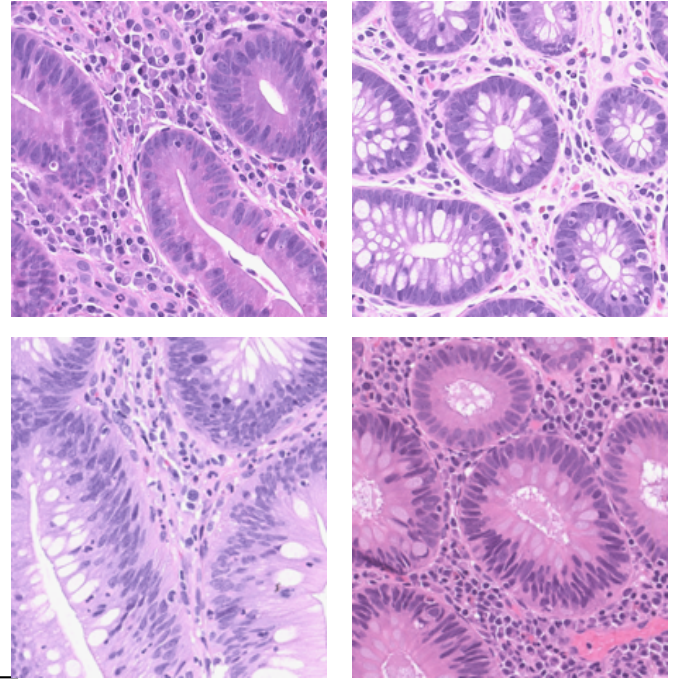


Fig. 5: Sample images of the dataset used: (a) H&E-stained WSI tiles from the case group consisting of tubular adenomas with low-grade dysplasia from patients who subsequently developed CRC (b) H&E-stained WSI tiles from the control group consisting of tubular adenomas with low-grade dysplasia from patients without subsequent development of CRC.

The original whole slide images (WSIs) were tiled at 1024×1024 pixel resolution with 3 color channels. They were then resized into smaller tiles of 224×224 pixels with 3 color channels for model input as shown in Fig. 5. During preprocessing, a region-of-interest (ROI) filter was applied to determine whether each tile should be retained or discarded. All automatically generated ROIs were subsequently subjected to visual inspection to verify annotation accuracy. Tiles exhibiting quality issues—such as tissue folding, edge artifacts, or poor scan resolution—were excluded through manual review of WSI patch location maps. After this curation process, a total of 135,049 high-quality tiles were retained in each class. The final dataset was divided into training (70%), validation (15%), and testing (15%) subsets.

1) Data Management Strategies: Patients without known high-risk clinical factors for CRC, in which low-grade tubular adenomas were identified during screening colonoscopy, were included in the study. A total of 81 patients (41 male, 40 female), ranging in age from 54–95 years (average 70), underwent at least one screening colonoscopy with associated biopsies demonstrating tubular adenomas with low-grade dysplasia; no biopsies showed any histologic features that were indicative of high-risk progression to CRC. Patients were stratified

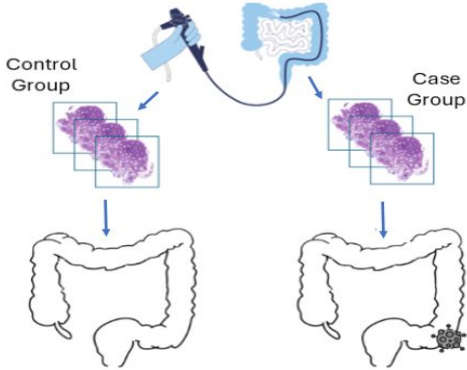


Fig. 6: Control Group: TA images from patients with no CRC development during follow-up. Case Group: TA images from patients who later developed CRC.

into two cohorts: a precancer group and a control group. The case group consisted of individuals who subsequently developed CRC following screening colonoscopies in which low-grade tubular adenomas were identified. The control group comprised of individuals with no history of CRC despite having low-grade adenomas detected on one or more screening procedures. Compared to the case group, the control group had a greater average number of biopsies and a longer mean screening interval. On average, patients in the case group were 6.86 years older than those in the control group. Histologic slides from both groups containing low-grade tubular adenomas were digitized using the same Leica Aperio AT2 whole slide scanner to generate image data for this study. Fig. 6 displays the pictorial details of the two cohorts: control group and case group.

C. Results

TABLE II: Quantitative performances of Transformer-based models, mamba-based models with linear and fixed non-negative orthogonal classifiers.

Models	Accuracy	F1	Precision	Recall
Transformer-Based Models				
Vision Transformer	89.84%	0.8920	0.9519	0.8392
Swin Transformer	89.52%	0.8878	0.9548	0.8296
Mamba-Based Models with Linear Classifier				
Conv. based	94.24%	0.9431	0.9324	0.9540
MBConv. based	92.44%	0.9221	0.9512	0.8948
Fused MBCConv. based	93.67%	0.9388	0.9076	0.9703
ConvNext based	96.50%	0.9651	0.9606	0.9697
XtraLight Mamba Models				
Conv. based	93.64%	0.9367	0.9321	0.9414
MBConv. based	93.96%	0.9117	0.9029	0.8913
Fused MBCConv. based	94.24%	0.9416	0.9547	0.9289
ConvNext based (ours, XtraLight-MedMamba)	97.18%	0.9767	0.9666	0.9717

Table II summarizes the quantitative performance of Transformer-based architectures, Mamba-based variants, and XtraLight Mamba-based variants, employing both linear and fixed non-negative orthogonal classifiers. Among the Transformer models, which primarily utilize self-attention mechanisms to capture long-range dependencies across image patches, the Vision Transformer achieved

an overall accuracy of 89.84% ($F1 = 0.8920$, precision = 0.9519, recall = 0.8392) with 7.39M parameters, while the Swin Transformer attained a comparable accuracy of 89.52% ($F1 = 0.8878$, precision = 0.9548, recall = 0.8296) using a more compact 598K parameters.

In comparison, the Mamba-based models built upon State Space Models (SSMs) that process sequential representations bidirectionally, demonstrated consistently higher performance with substantially fewer parameters. Within the linear classifier group, the ConvNeXt-based Mamba variant achieved the highest accuracy of 96.50% ($F1 = 0.9651$, precision = 0.9606, recall = 0.9697), outperforming the convolutional, MBConv, and Fused MBCConv variants. The incorporation of the SCAB module further enhanced feature propagation, which proved beneficial for the image classification task. As the SSM effectively models hidden states over time, it excels at capturing both long- and short-range dependencies within spatial representations.

Similarly, the proposed XtraLight Mamba models maintained strong performance while significantly reducing model complexity. Our model, ConvNeXt-based XtraLight-MedMamba, achieved the best overall results, reaching an accuracy of 97.18% ($F1 = 0.9767$, precision = 0.9666, recall = 0.9717) with only 32K parameters, surpassing all other tested configurations. These findings highlight that integrating ConvNeXt-style inverted bottlenecks within the Mamba framework provides an optimal balance between efficiency and accuracy, outperforming both Transformer and other Mamba variants.

Table III presents the normalized confusion matrix for the proposed XtraLight-MedMamba model. The classifier achieved exceptionally high discriminative performance, correctly identifying 97.7% of positive samples (true positives) and 96.7% of negative samples (true negatives). Only a small fraction of the cases were misclassified, with 2.3% false negatives and 3.3% false positives. These results demonstrate the strong sensitivity and specificity of the model, confirming its robustness and reliability in distinguishing between positive and negative classes. The high diagonal dominance of the matrix further reflects the effectiveness of the learned feature representations and the generalizability of the model throughout the dataset.

TABLE III: Confusion matrix for XtraLight-MedMamba

	Predicted Positive	Predicted Negative
Actual Positive	0.9770 (TP)	0.0230 (FN)
Actual Negative	0.0333 (FP)	0.9667 (TN)

D. Model Interpretability and Visual Explanation

To aid interpretation of the decision-making behavior of the proposed XtraLight-MedMamba model, Gradient-weighted Class Activation Mapping (Grad-CAM) [61] was used to visualize the spatial regions contributing most strongly to classification. As illustrated in Fig. 7, the generated activation maps highlight the discriminative

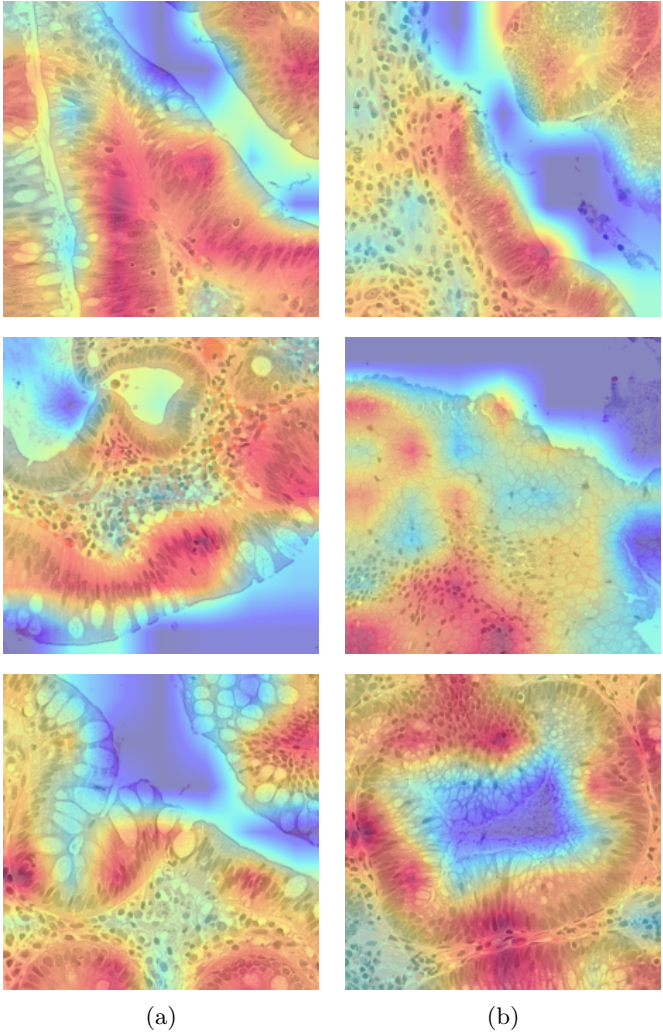


Fig. 7: Grad-CAM based visualization of particular regions learned by the proposed XtraLight-MedMamba model. (a) Case samples highlight increased activation over the epithelium with subtle architectural and cytologic irregularities. (b) Control samples show diffuse attention across well-organized glandular structures, suggesting reliance on biologically relevant features.

tissue areas that influenced the model’s predictions. Regions with warmer colors (red–yellow) correspond to areas of greater interest, whereas cooler colors (blue–purple) indicate lesser contribution. The Grad-CAM overlays demonstrate that the network predominantly focuses on histologically relevant structures—such as atypical epithelial glands, nuclear crowding, and stromal interfaces—rather than background artifacts. This highlights how model activations and pathologically significant features support the interpretability and reliability of the model, confirming that XtraLight-MedMamba learns clinically meaningful representations rather than false correlations.

A closer look at the Grad-CAM visualizations in Fig. 7 shows that the model’s attention is drawn mainly to nuclear architecture. In both case and control images, the highlighted regions consistently align with ar-

eas rich in nuclear material, especially where the nuclei appear pseudostratified or show subtle irregularities in their basal orientation. In case samples, these activations often correspond to regions with more pronounced pseudostratification and occasional loss or disorder of polarity, while control samples display well-aligned nuclei with layering to case nuclei. Together, these observations suggest that XtraLight-MedMamba differentiates tissues primarily by recognizing patterns of nuclear arrangement and polarity—the same microscopic cues pathologists use to identify epithelial atypia and assess disease progression.

E. Mismatched predicted outputs of XtraLight-MedMamba

In Fig. 8 (a), the patch clearly demonstrates morphological features of tubular adenoma: nuclear pseudostratification, hyperchromatic elongated nuclei, and goblet cell depletion. Despite the morphologic hallmarks being present, the model misclassified this region as class control. This could reflect the model’s limited sensitivity to focal dysplasia, particularly in areas with mixed histology, where adjacent non-dysplastic crypts can mask subtle neoplastic changes. These results highlight the need for enhanced model training with finer-grained annotations and increased representation of early or borderline dysplasia cases.

In Fig. 8 (b), the region is histologically consistent with slight adenomatous changes from the control group and was misclassified by the model as a tubular adenoma that progressed to CRC (case group). The crypts are well-formed, with preserved spacing, abundant goblet cells, and basally aligned nuclei, lacking pseudostratification, along with no cytologic atypia indicative of a high-grade dysplasia. Morphologically, there are no other signs of progression to CRC. This false positive might be due to subtle visual cues such as epithelial overcrowding near the tissue edge or darker nuclear staining, which the model may overfit during training.

V. CONCLUSION

In this work, we introduced XtraLight-MedMamba, an extra lightweight state-space model for the classification of Neoplastic Tubular Adenomas (NPTA). The proposed architecture is a combination of ConvNext blocks for shallow feature extraction with PVM layers to efficiently capture both short- and long-range dependencies while maintaining a minimal parameter footprint. The performance was further improved by integrating SCAB module and FNOclassifier. The proposed approach achieved enhanced classification performance on a curated dataset of low-grade tubular adenomas, which outperformed transformer-based and conventional Mamba architectures with substantially fewer parameters. Grad-CAM analysis demonstrated that the network captured subtle histological patterns, including nuclear architecture and epithelial atypia, supporting both interpretability and clinical relevance, by highlighting discriminative feature that conventional methods may overlook.

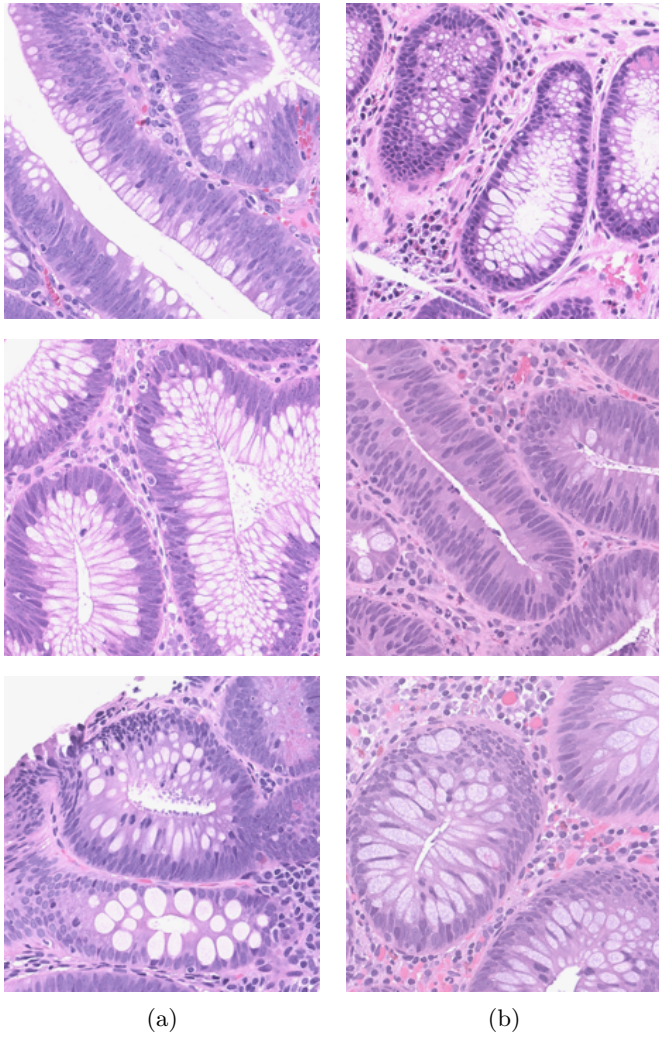


Fig. 8: Representative mismatched predictions made by XtraLight-MedMamba. (a) Target: Case, Predicted: Control. The glands in these sections show preserved architecture with evenly spaced crypts and relatively consistent nuclear alignment. Cytologic atypia in these sections are subtle, showing mild nuclear enlargement and crowding, morphological features closely resembling low-risk tubular adenomas. The lack of overt glandular complexity or pronounced dysplasia likely contributed to the model misclassifying the sample as Control. (b) Target: Control, Predicted: Case. In contrast, these Control samples exhibit focal areas of gland crowding, mild loss of polarity, and mild pseudostratification of the nuclei with darker nuclei. These morphological patterns tend to be more commonly associated with higher-risk lesions, which may have led the model to weigh these as Case associated features.

ACKNOWLEDGMENT

The authors acknowledge the South Bend Medical Foundation (SBMF) team for their support in providing access to the Neoplastic Tubular Adenomas dataset.

REFERENCES

- [1] A. C. Society, “Cancer facts and figures 2025,” 2025, american Cancer Society, Atlanta, GA, USA. [Online]. Available: Available:<https://www.cancer.org/research/cancer-facts-statistics.html>, [Online].
- [2] R. L. Siegel, A. N. Giaquinto, and A. Jemal, “Cancer statistics, 2024,” CA: A Cancer Journal for Clinicians, vol. 74, no. 1, pp. 12–49, 2024. [Online]. Available: <https://acsjournals.onlinelibrary.wiley.com/doi/abs/10.3322/caac.21820>
- [3] J. Rosai, Rosai and Ackerman’s Surgical Pathology, 10e, 10th ed. Elsevier, Jul. 2011, vol. 1.
- [4] American Cancer Society Colorectal Cancer Advisory Group, US Multi-Society Task Force on Colorectal Cancer, American College of Radiology Colon Cancer Committee, B. Levin, D. A. Lieberman, B. McFarland, K. S. Andrews, D. Brooks, J. Bond, C. Dash, F. M. Giardiello, S. Glick, D. Johnson, C. D. Johnson, T. R. Levin, P. J. Pickhardt, D. K. Rex, R. A. Smith, A. Thorson, and S. J. Winawer, “Screening and surveillance for the early detection of colorectal cancer and adenomatous polyps, 2008: A joint guideline from the american cancer society, the US multi-society task force on colorectal cancer, and the american college of radiology,” Gastroenterology, vol. 134, no. 5, pp. 1570–1595, 2008.
- [5] B. Vogelstein, E. R. Fearon, S. R. Hamilton, S. E. Kern, A. C. Preisinger, M. Leppert, A. M. Smits, and J. L. Bos, “Genetic alterations during colorectal-tumor development,” New England Journal of Medicine, vol. 319, no. 9, pp. 525–532, 1988. [Online]. Available: <https://www.nejm.org/doi/full/10.1056/NEJM198809013190901>
- [6] U. P. S. T. Force, “Screening for colorectal cancer: Us preventive services task force recommendation statement,” JAMA, vol. 325, no. 19, p. 1965–1977, May 2021. [Online]. Available: <https://doi.org/10.1001/jama.2021.6238>
- [7] M. Øines, L. M. Helsingør, M. Brethauer, and L. Emilsson, “Epidemiology and risk factors of colorectal polyps,” Best Practice and Research Clinical Gastroenterology, vol. 31, no. 4, pp. 419–424, 2017, gastrointestinal Polyps. [Online]. Available: <https://www.sciencedirect.com/science/article/pii/S1521691817300677>
- [8] G. Litjens, T. Kooi, B. E. Bejnordi, A. A. A. Setio, F. Ciompi, M. Ghafoorian, J. A. van der Laak, B. van Ginneken, and C. I. Sánchez, “A survey on deep learning in medical image analysis,” Medical Image Analysis, vol. 42, pp. 60–88, 2017. [Online]. Available: <https://www.sciencedirect.com/science/article/pii/S1361841517301135>
- [9] A. Madabhushi and G. Lee, “Image analysis and machine learning in digital pathology: Challenges and opportunities,” Medical Image Analysis, vol. 33, pp. 170–175, 2016, 20th anniversary of the Medical Image Analysis journal (MEDIA). [Online]. Available: <https://www.sciencedirect.com/science/article/pii/S1361841516301141>
- [10] K. O’Shea and R. Nash, “An introduction to convolutional neural networks,” 2015. [Online]. Available: <https://arxiv.org/abs/1511.08458>
- [11] K. He, X. Zhang, S. Ren, and J. Sun, “Deep Residual Learning for Image Recognition,” in 2016 IEEE Conference on Computer Vision and Pattern Recognition (CVPR). Las Vegas, NV, USA: IEEE, Jun. 2016, pp. 770–778. [Online]. Available: <http://ieeexplore.ieee.org/document/7780459/>
- [12] M. Liang and X. Hu, “Recurrent convolutional neural network for object recognition,” in 2015 IEEE Conference on Computer Vision and Pattern Recognition (CVPR), 2015, pp. 3367–3375.
- [13] M. Tan and Q. V. Le, “Efficientnetv2: Smaller models and faster training,” 2021. [Online]. Available: <https://arxiv.org/abs/2104.00298>
- [14] Z. Liu, Y. Lin, Y. Cao, H. Hu, Y. Wei, Z. Zhang, S. Lin, and B. Guo, “Swin transformer: Hierarchical vision transformer using shifted windows,” CoRR, vol. abs/2103.14030, 2021. [Online]. Available: <https://arxiv.org/abs/2103.14030>
- [15] A. Dosovitskiy, L. Beyer, A. Kolesnikov, D. Weissenborn, X. Zhai, T. Unterthiner, M. Dehghani, M. Minderer, G. Heigold, S. Gelly, J. Uszkoreit, and N. Houlsby, “An image is worth 16x16 words: Transformers for image recognition at scale,” CoRR, vol. abs/2010.11929, 2020. [Online]. Available: <https://arxiv.org/abs/2010.11929>

[16] A. Gu, K. Goel, and C. Ré, "Efficiently modeling long sequences with structured state spaces," 2022. [Online]. Available: <https://arxiv.org/abs/2111.00396>

[17] A. Gu and T. Dao, "Mamba: Linear-time sequence modeling with selective state spaces," 2024. [Online]. Available: <https://arxiv.org/abs/2312.00752>

[18] L. Zhu, B. Liao, Q. Zhang, X. Wang, W. Liu, and X. Wang, "Vision mamba: Efficient visual representation learning with bidirectional state space model," 2024. [Online]. Available: <https://arxiv.org/abs/2401.09417>

[19] M. M. Rahman, A. A. Tutul, A. Nath, L. Laishram, S. K. Jung, and T. Hammond, "Mamba in vision: A comprehensive survey of techniques and applications," 2024. [Online]. Available: <https://arxiv.org/abs/2410.03105>

[20] A. Sultana, S. N. Abouzahra, V. K. Asari, T. Aspiras, R. Liu, I. Sudakow, and L. Cooper, "Ultralight visionmamba unet: a segmentation architecture for meltpond region localization," in *Pattern Recognition and Prediction XXXVI*, M. S. Alam and V. K. Asari, Eds., vol. 13464. SPIE, 2025, p. 134640N, backup Publisher: International Society for Optics and Photonics. [Online]. Available: <https://doi.org/10.1117/12.3054674>

[21] A. Sultana, N. Abouzahra, A. Rahu, B. Shula, B. Combs, D. Forchetti, T. Aspiras, and V. K. Asari, "Ultralight med-vision mamba for classification of neoplastic progression in tubular adenomas," in *NAECON 2025 - IEEE National Aerospace and Electronics Conference*, 2025, pp. 1–6.

[22] A. Dosovitskiy, L. Beyer, A. Kolesnikov, D. Weissenborn, X. Zhai, T. Unterthiner, M. Dehghani, M. Minderer, G. Heigold, S. Gelly, J. Uszkoreit, and N. Houlsby, "An Image is Worth 16x16 Words: Transformers for Image Recognition at Scale," Jun. 2021, arXiv:2010.11929 [cs]. [Online]. Available: <https://arxiv.org/abs/2010.11929>

[23] P. W. Hamilton, P. H. Bartels, D. Thompson, N. H. Anderson, R. Montironi, and J. M. Sloan, "Automated Location of Dysplastic Fields in Colorectal Histology Using Image Texture Analysis," *The Journal of Pathology*, vol. 182, no. 1, pp. 68–75, 1997, _eprint: <https://pathsocjournals.onlinelibrary.wiley.com/doi/pdf/10.1002/%28SICI%9896%28199705%29182%3A1%3C68%3A%3AAID-PATH811%3E3.0.CO%3B2-N>. [Online]. Available: <https://onlinelibrary.wiley.com/doi/abs/10.1002/%28SICI%291096-9896%28199705%29182%3A1%3C68%3A%3AAID-PATH811%3E3.0.CO%3B2-N>

[24] H. Kalkan, M. Nap, R. P. W. Duin, and M. Loog, "Automated Colorectal Cancer Diagnosis for Whole-Slice Histopathology," in *Medical Image Computing and Computer-Assisted Intervention – MICCAI 2012*, N. Ayache, H. Delingette, P. Golland, and K. Mori, Eds. Berlin, Heidelberg: Springer, 2012, pp. 550–557.

[25] N. Sengar, N. Mishra, M. K. Dutta, J. Prinosil, and R. Burget, "Grading of colorectal cancer using histology images," in *2016 39th International Conference on Telecommunications and Signal Processing (TSP)*, Jun. 2016, pp. 529–532. [Online]. Available: <https://ieeexplore.ieee.org/document/7760936>

[26] J. N. Kather, C.-A. Weis, F. Bianconi, S. M. Melchers, L. R. Schad, T. Gaiser, A. Marx, and F. G. Zöllner, "Multi-class texture analysis in colorectal cancer histology," *Scientific Reports*, vol. 6, p. 27988, Jun. 2016. [Online]. Available: <https://pmc.ncbi.nlm.nih.gov/articles/PMC4910082/>

[27] A. Krizhevsky, I. Sutskever, and G. E. Hinton, "ImageNet Classification with Deep Convolutional Neural Networks," in *Advances in Neural Information Processing Systems*, vol. 25. Curran Associates, Inc., 2012. [Online]. Available: <https://proceedings.neurips.cc/paper/2012/hash/c399862d3b9d6b76c8436e924a68c45b-Abstract.html>

[28] A. Ben Hamida, M. Devanne, J. Weber, C. Truntzer, V. Derangère, F. Ghiringhelli, G. Forestier, and C. Wemmert, "Deep learning for colon cancer histopathological images analysis," *Computers in Biology and Medicine*, vol. 136, p. 104730, Sep. 2021. [Online]. Available: <https://linkinghub.elsevier.com/retrieve/pii/S0010482521005242>

[29] A. Davri, E. Birbas, T. Kanavos, G. Ntritsos, N. Giannakeas, A. T. Tzallas, and A. Batistatou, "Deep Learning on Histopathological Images for Colorectal Cancer Diagnosis: A Systematic Review," *Diagnostics*, vol. 12, no. 4, Mar. 2022. [Online]. Available: <https://www.mdpi.com/2075-4418/12/4/837>

[30] Z. Song, C. Yu, S. Zou, W. Wang, Y. Huang, X. Ding, J. Liu, L. Shao, J. Yuan, X. Gou, W. Jin, Z. Wang, X. Chen, H. Chen, C. Liu, G. Xu, Z. Sun, C. Ku, Y. Zhang, X. Dong, S. Wang, W. Xu, N. Lv, and H. Shi, "Automatic deep learning-based colorectal adenoma detection system and its similarities with pathologists," *BMJ Open*, vol. 10, no. 9, p. e036423, Sep. 2020. [Online]. Available: <https://bmjopen.bmjjournals.org/content/10/9/e036423>

[31] K. S. Wang, G. Yu, C. Xu, X. H. Meng, J. Zhou, C. Zheng, Z. Deng, L. Shang, R. Liu, S. Su, X. Zhou, Q. Li, J. Li, J. Wang, K. Ma, J. Qi, Z. Hu, P. Tang, J. Deng, X. Qiu, B. Y. Li, W. D. Shen, R. P. Quan, J. T. Yang, L. Y. Huang, Y. Xiao, Z. C. Yang, Z. Li, S. C. Wang, H. Ren, C. Liang, W. Guo, Y. Li, H. Xiao, Y. Gu, J. P. Yun, D. Huang, Z. Song, X. Fan, L. Chen, X. Yan, Z. Li, Z. C. Huang, J. Huang, J. Luttrell, C. Y. Zhang, W. Zhou, K. Zhang, C. Yi, C. Wu, H. Shen, Y. P. Wang, H. M. Xiao, and H. W. Deng, "Accurate diagnosis of colorectal cancer based on histopathology images using artificial intelligence," *BMC Medicine*, vol. 19, no. 1, p. 76, Mar. 2021. [Online]. Available: <https://doi.org/10.1186/s12916-021-01942-5>

[32] I. Haq, T. Mazhar, R. N. Asif, Y. Y. Ghadi, N. Ullah, M. A. Khan, and A. Al-Rasheed, "YOLO and residual network for colorectal cancer cell detection and counting," *Heliyon*, vol. 10, no. 2, Jan. 2024. [Online]. Available: [https://www.cell.com/heliyon/abstract/S2405-8440\(24\)00434-1](https://www.cell.com/heliyon/abstract/S2405-8440(24)00434-1)

[33] X. Zhou, Y. Lu, Y. Wu, Y. Yu, Y. Liu, C. Wang, Z. Zhao, C. Wang, Z. Gao, Z. Li, Y. Zhao, and W. Cao, "Construction and validation of a deep learning prognostic model based on digital pathology images of stage III colorectal cancer," *European Journal of Surgical Oncology*, vol. 50, no. 7, p. 108369, Jul. 2024. [Online]. Available: <https://linkinghub.elsevier.com/retrieve/pii/S0748798324004219>

[34] N. Trahearn, C. Sakr, A. Banerjee, S. H. Lee, A.-M. Baker, H. M. Kocher, V. Angerilli, F. Morano, F. Bergamo, G. Maddalena, R. Intini, C. Cremolini, G. Caravagna, T. Graham, F. Pietrantonio, S. Lonardi, M. Fassan, and A. Sottoriva, "Computational pathology applied to clinical colorectal cancer cohorts identifies immune and endothelial cell spatial patterns predictive of outcome," *The Journal of Pathology*, vol. 265, no. 2, pp. 198–210, 2025, _eprint: <https://pathsocjournals.onlinelibrary.wiley.com/doi/pdf/10.1002/path.6378>. [Online]. Available: <https://onlinelibrary.wiley.com/doi/abs/10.1002/path.6378>

[35] E. Steimetz, Z. C. Simsek, A. Saha, R. Xia, and R. Gupta, "Deep learning model for detecting high-grade dysplasia in colorectal adenomas," *Journal of Pathology Informatics*, vol. 17, p. 100441, Apr. 2025. [Online]. Available: <https://linkinghub.elsevier.com/retrieve/pii/S2153353925000264>

[36] J. Kim, N. Tomita, A. A. Suriawinata, and S. Hassanpour, "Detection of Colorectal Adenocarcinoma and Grading Dysplasia on Histopathologic Slides Using Deep Learning," *The American Journal of Pathology*, vol. 193, no. 3, pp. 332–340, Mar. 2023. [Online]. Available: <https://linkinghub.elsevier.com/retrieve/pii/S0002944022003996>

[37] D. Perlo, E. Tartaglione, L. Bertero, P. Cassoni, and M. Grangetto, "Dysplasia Grading of Colorectal Polyps Through Convolutional Neural Network Analysis of Whole Slide Images," in *Proceedings of 2021 International Conference on Medical Imaging and Computer-Aided Diagnosis (MICAD 2021)*, R. Su, Y.-D. Zhang, and H. Liu, Eds. Singapore: Springer, 2022, pp. 325–334.

[38] B. Sathyaranayana, S. Alampally, R. Akella, and V. V. R. Indugu, "ColoViT: a synergistic integration of EfficientNet and vision transformers for advanced colon cancer detection," *Journal of Cancer Research and Clinical Oncology*, vol. 151, no. 7, p. 209, Jul. 2025. [Online]. Available: <https://doi.org/10.1007/s00432-025-06199-6>

[39] R. T. P., J. Kumar, and S. R. Balasundaram, "DeepCPD: deep learning with vision transformer for colorectal polyp detection," *Multimedia Tools and Applications*, vol. 83, no. 32, pp. 78183–78206, Sep. 2024. [Online]. Available: <https://doi.org/10.1007/s11042-024-18607-z>

[40] Z. Qin, W. Sun, T. Guo, and G. Lu, "Colorectal cancer image recognition algorithm based on improved transformer," *Discover Applied Sciences*, vol. 6, no. 8, p. 422, Aug. 2024. [Online]. Available: <https://doi.org/10.1007/s42452-024-06127-2>

[41] M. Le Rochais, I. Brahim, R. Zeghlache, G. Redoulez, M. Guillard, P. Le Noac'h, M. Castillon, A. Bourhis, and A. Uguen, "Automated classification of tertiary lymphoid structures in colorectal cancer using TLS-PAT artificial intelligence tool," *Scientific Reports*, vol. 15, no. 1, p. 9845, Mar. 2025. [Online]. Available: <https://www.nature.com/articles/s41598-025-94664-0>

[42] Y.-C. Chen, T. Chao, W. N. Phandita, T.-Y. Sun, H.-Z. Wang, Y.-H. Hsieh, L.-Y. Hsu, and C. Lin, "Predicting Microsatellite Instability from Histology Images with Dilated Neighborhood Attention Transformer in Colorectal Cancer," in 2024 IEEE 24th International Conference on Bioinformatics and Bioengineering (BIBE), Nov. 2024, pp. 1–5. [Online]. Available: <https://ieeexplore.ieee.org/abstract/document/10820458>

[43] F. D. Keles, P. M. Wijewardena, and C. Hegde, "On The Computational Complexity of Self-Attention," in Proceedings of The 34th International Conference on Algorithmic Learning Theory. PMLR, Feb. 2023, pp. 597–619. [Online]. Available: <https://proceedings.mlr.press/v201/duman-keles23a.html>

[44] J. Zhang, A. T. Nguyen, X. Han, V. Q.-H. Trinh, H. Qin, D. Samaras, and M. S. Hosseini, "2DMamba: Efficient State Space Model for Image Representation with Applications on Giga-Pixel Whole Slide Image Classification," 2025, pp. 3583–3592. [Online]. Available: https://openaccess.thecvf.com/content/CVPR2025/html/Zhang_2DMamba_Efficient_State_Space_Model_for_Image_Representation_with_Applications_CVPR_2025_paper.html

[45] T. Zheng, K. Jiang, Y. Xiao, S. Zhao, and H. Yao, "M3amba: Memory Mamba is All You Need for Whole Slide Image Classification," 2025, pp. 15 601–15 610. [Online]. Available: https://openaccess.thecvf.com/content/CVPR2025/html/Zheng_M3amba_Memory_Mamba_is_All_You_Need_for_Whole_Slide_CVPR_2025_paper.html

[46] R. Ding, K.-D. Luong, E. Rodriguez, A. C. A. L. da Silva, and W. Hsu, "Combining graph neural network and Mamba to capture local and global tissue spatial relationships in whole slide images," *Scientific Reports*, vol. 15, no. 1, p. 18261, May 2025. [Online]. Available: <https://www.nature.com/articles/s41598-025-99042-4>

[47] S. Khan, F. Dambandkhameh, N. Shaikh, Y. Nie, R. Venugopal, and X. Li, "SlideMamba: entropy-based adaptive fusion of GNN and Mamba for enhanced representation learning in digital pathology," *Scientific Reports*, Jan. 2026. [Online]. Available: <https://www.nature.com/articles/s41598-025-34367-8>

[48] A. Malekmohammadi, A. Badiezadeh, S. M. Mirhassani, P. Gifani, and M. Vafaeezadeh, "Classification of Gleason Grading in Prostate Cancer Histopathology Images Using Deep Learning Techniques: YOLO, Vision Transformers, and Vision Mamba," Oct. 2024, arXiv:2409.17122 [eess]. [Online]. Available: <http://arxiv.org/abs/2409.17122>

[49] A. Nasiri-Sarvi, V. Q.-H. Trinh, H. Rivaz, and M. S. Hosseini, "Vim4Path: Self-Supervised Vision Mamba for Histopathology Images," 2024, pp. 6894–6903. [Online]. Available: https://openaccess.thecvf.com/content/CVPR2024W/CVMI/html/Nasiri-Sarvi_Vim4Path_Self-Supervised_Vision_Mamba_for_Histopathology_Images_CVPRW_2024_paper.html

[50] X. Zhu, S. Zhang, H. Hao, and Y. Zhao, "Adversarial-based latent space alignment network for left atrial appendage segmentation in transesophageal echocardiography images," *Frontiers in Cardiovascular Medicine*, vol. 10, p. 1153053, 03 2023.

[51] Z. Liu, H. Mao, C.-Y. Wu, C. Feichtenhofer, T. Darrell, and S. Xie, "A convnet for the 2020s," in Proceedings of the IEEE/CVF Conference on Computer Vision and Pattern Recognition (CVPR), June 2022, pp. 11 976–11 986.

[52] R. Wu, Y. Liu, P. Liang, and Q. Chang, "Ultralight vmmunet: Parallel vision mamba significantly reduces parameters for skin lesion segmentation," 2024. [Online]. Available: <https://arxiv.org/abs/2403.20035>

[53] J. Ruan, S. Xiang, M. Xie, T. Liu, and Y. Fu, "Malunet: A multi-attention and light-weight unet for skin lesion segmentation," 2022. [Online]. Available: <https://arxiv.org/abs/2211.01784>

[54] H. Kim and K. Kim, "Fixed non-negative orthogonal classifier: Inducing zero-mean neural collapse with feature dimension separation," in The Twelfth International Conference on Learning Representations, 2024. [Online]. Available: <https://openreview.net/forum?id=F4bmOrmUwc>

[55] C. Xu, X. Li, and M. Yang, "An orthogonal classifier for improving the adversarial robustness of neural networks," *Information Sciences*, vol. 591, pp. 251–262, 2022. [Online]. Available: <https://www.sciencedirect.com/science/article/pii/S0020020522000627>

[56] V. Papyan, X. Y. Han, and D. L. Donoho, "Prevalence of neural collapse during the terminal phase of deep learning training," *Proceedings of the National Academy of Sciences*, vol. 117, no. 40, p. 24652–24663, Sep. 2020. [Online]. Available: <http://dx.doi.org/10.1073/pnas.2015509117>

[57] J. Jiang, J. Zhou, P. Wang, Q. Qu, D. Mixon, C. You, and Z. Zhu, "Generalized neural collapse for a large number of classes," 2023. [Online]. Available: <https://arxiv.org/abs/2310.05351>

[58] Z. Chen, M. Zhang, S. Cui, H. Li, G. Niu, M. Gong, C. Zhang, and K. Zhang, "Neural collapse inspired feature alignment for out-of-distribution generalization," in The Thirty-eighth Annual Conference on Neural Information Processing Systems, 2024. [Online]. Available: <https://openreview.net/forum?id=wQpNG9JnPK>

[59] D. Soudry, E. Hoffer, M. S. Nacson, S. Gunasekar, and N. Srebro, "The implicit bias of gradient descent on separable data," 2024. [Online]. Available: <https://arxiv.org/abs/1710.10345>

[60] Z. Zhu, T. Ding, J. Zhou, X. Li, C. You, J. Sulam, and Q. Qu, "A geometric analysis of neural collapse with unconstrained features," 2021. [Online]. Available: <https://arxiv.org/abs/2105.02375>

[61] R. R. Selvaraju, M. Cogswell, A. Das, R. Vedantam, D. Parikh, and D. Batra, "Grad-cam: Visual explanations from deep networks via gradient-based localization," *International Journal of Computer Vision*, vol. 128, no. 2, p. 336–359, Oct. 2019. [Online]. Available: <http://dx.doi.org/10.1007/s11263-019-01228-7>

VI. BIOGRAPHY SECTION



Aqsa Sultana (Student Member, IEEE) has a Master's degree in Computer Engineering and is currently pursuing her PhD in Electrical Engineering at the University of Dayton. Her research interests encompass remote sensing applications, neuromorphic computing/spiking neural networks, automated feature extraction, and pattern recognition algorithms for oncology.



Rayan Afsar (Student Member, IEEE) is currently pursuing his Bachelor's degree in Computer Science at the University of Georgia. His research interests revolve around integrating computer vision with remote sensing to aid human-based decision making and to validate environmental models for understanding Earth systems.



Ahmed Rahu, MD received his B.S. in Biomedical Engineering from George Mason University, Fairfax, VA, and earned his M.D. from Ross University School of Medicine. He is currently a PGY-2 Pathology resident at the University of Toledo Medical Center. His academic and clinical interests center on bridging technology and medicine to advance disease prevention, diagnostic precision, and therapeutic innovation. His research focuses on digital pathology, computational pathology, and machine-learning-based image analysis, with particular interest in risk stratification of pre-malignant lesions, predictive modeling in oncologic pathology, and the development of lightweight, interpretable deep learning architectures for clinical deployment.



Surendra P. Singh, MD joined the Consultants in Laboratory Medicine in 2000 and had various roles including Medical Director/Vice Chairman in Anatomic Pathology, Microbiology, Medical Education and ProMedica BioRepository. He is board certified in anatomic and clinical pathology. He completed a Gastrointestinal pathology fellowship at Harvard Medical School /Beth Israel Deaconess Medical Center, Boston. He completed his Anatomic and Clinical Pathology residency and a Surgical Pathology fellowship at the Ohio State University. He also completed an American Cancer Society Fellowship in Clinical Oncology at The Ohio State University. He received his graduate M.B; B.S degree and postgraduate M.D degrees from the M.S University and Medical College of Baroda, India. Dr. Singh maintains a faculty appointment at the College of Medicine and Life Sciences, University of Toledo as a Clinical Associate Professor. He also chairs the Aurora GI and Liver Council. He has authored several articles in peer reviewed journals and has received numerous awards including Stowell Orbison Award. His primary interest includes general surgical, gastrointestinal and liver and oncologic pathology, immunohistochemistry, microbiology and infectious pathology, and medical education.



Brian Shula is a Lead Mechanical Design Engineer for Aircraft Wheels and Brakes at Honeywell, with over 20 years of structural numerical simulation experience, predominantly in the aerospace industry. Brian has applied machine learning tools in structural simulation settings by developing finite element surrogate models to facilitate design space exploration. Mr. Shula earned his BSME and MSME from the University of Notre Dame and holds a Professional Engineer license in Ohio.



Brandon Combs is a Cisco-certified Technical Solutions Architect at the South Bend Medical Foundation, where he has supported clinical laboratory operations and advanced digital pathology systems for over a decade, beginning as an independent contractor. He received Bachelor of Science degrees in Mathematics and Physics from Indiana University, followed by a Master of Science degree in Applied Mathematics and Computer Science.

His technical and research interests include computational pathology, automated image quality assessment, machine learning-based quality control, clinical workflow optimization, and scalable cloud-based healthcare systems. His professional experience spans software engineering, system architecture, and enterprise network administration for distributed clinical environments.



Derrick Forchetti, MD received a B.A. degree (cum laude) in chemistry and German from Wabash College in 1993, an M.D. degree from Indiana University School of Medicine in 1997, and an M.S. degree in data science from the University of Wisconsin Extended Campus in 2021. He completed a five-year residency training program in anatomic and clinical pathology at Ball Memorial Hospital in 2002.

He is a board-certified anatomic and clinical pathologist with nearly 25 years of practice experience, with additional board certification in clinical informatics. He currently serves as a pathologist at South Bend Medical Foundation and as a volunteer Assistant Professor at the University of Toledo College of Medicine and Life Sciences. He is a member of the College of American Pathologists Digital and Computational Pathology Committee. His research interests include automated quality control for whole slide imaging, digital pathology workflows, and the application of artificial intelligence in diagnostic laboratories.



Vijayan K. Asari, PhD (Senior Member, IEEE) received the Ph.D. degree in electrical engineering from the Indian Institute of Technology Madras, Chennai, India, in 1994. He is currently a Professor of Electrical and Computer Engineering and the Ohio Research Scholars Endowed Chair in wide area surveillance with the University of Dayton, Dayton, OH, USA, where he is also the Director of the Center of Excellence for Computational Intelligence and Machine Vision (Vision Lab).

He holds five U.S. patents and has published more than 800 research articles, including 147 peer-reviewed journal papers and 7 edited books co-authoring with his students, colleagues and collaborators in the areas of image processing, pattern recognition, machine learning, deep learning, and artificial neural networks. Dr. Asari is a recipient of several teaching, research, advising, and technical leadership awards, including the Outstanding Engineers and Scientists Award for Technical Leadership from The Affiliate Societies Council of Dayton in April 2015, the Sigma Xi George B. Noland Award for Outstanding Research in April 2016, and the University of Dayton School of Engineering Vision Award for Excellence in August 2017. Dr. Asari was selected as a Fulbright Specialist by the US Department of State's Bureau of Educational and Cultural Affairs (ECA) and World Learning in 2017. He was also selected as European Union's Erasmus+ Faculty Fellow in 2018. Professor Asari is a Senior Member of IEEE and an elected Fellow of SPIE, and a Co-Organizer of several IEEE and SPIE conferences and workshops.